



Proper Motions of Water Masers in W49 N Measured by KaVA

Kitiyanee Asanok¹, Malcolm D. Gray^{1,2}, Tomoya Hirota^{3,4}, Koichiro Sugiyama¹, Montree Phetra⁵,
Busaba H. Kramer^{1,6}, Tie Liu^{7,8}, Kee-Tae Kim⁸, and Bannawit Pimpanuwat²

¹National Astronomical Research Institute of Thailand, 260 Moo 4, Tambol Donkaew, Amphur Maerim, Chiang Mai, 50180, Thailand; kitiyanee@narit.or.th

²The University of Manchester, Jodrell Bank Centre for Astrophysics, School of Physics and Astronomy, Alan Turing Building, M139PL, UK

³Mizusawa VLBI Observatory, National Astronomical Observatory of Japan, Osawa 2-21-1, Mitaka-shi, Tokyo, 181-8588, Japan

⁴Department of Astronomical Sciences, SOKENDAI (The Graduate University for Advanced Studies), Osawa 2-21-1, Mitaka-shi, Tokyo, 181-8588, Japan

⁵Graduate School, Department of Physics and Material Science, Faculty of Science, Chiang Mai University, Chiang Mai, 50200, Thailand

⁶Max-Planck-Institut für Radioastronomie, Auf dem Hügel 69, Bonn, D-53121, Germany

⁷Shanghai Astronomical Observatory, Chinese Academy of Sciences, 80 Nandan Road, Shanghai, 200030, People's Republic of China

⁸Korea Astronomy and Space Science Institute, 776 Daedeokdae-ro, Yuseong-gu, Daejeon, 34055, Republic of Korea

Received 2022 August 25; revised 2022 November 24; accepted 2022 November 25; published 2023 January 27

Abstract

We report the proper motions of 22 GHz water masers toward W49 N that were observed by the KVN and VERA Array (KaVA) during 2017 February–May. We found 263, 268, and 310 features in three successive epochs; they were distributed in a region of size 4×4 arcsec². The strongest flux density was in the third epoch, and its averaged value was 18,090 Jy at $V_{\text{LSR}} + 0.47$ km s⁻¹. For 102 H₂O maser features, proper motion was detected across all three epochs. The average proper motions in R.A. and decl. offset were -0.352 and $+0.890$ mas yr⁻¹, respectively. The morphology of the distribution of the H₂O maser features was found to be a bipolar outflow structure with an inclination angle of $37^\circ \pm 13^\circ$ to the line of sight, and the features were expanding from a well-defined outflow center. A model of the source combining expansion and rotation yielded a distance to W49 of 11.12 ± 0.96 kpc that is consistent with the results from trigonometric parallax. A redshifted lobe was situated in the northeast direction and a blueshifted lobe in the southwest direction. We also discussed the location of the powerful flaring H₂O maser feature at $V_{\text{LSR}} = +6$ km s⁻¹ and its possible mechanisms on the basis of spatial structures for the maser feature in VLBI maps observed with the KaVA, timed just before and during the rebrightening phase.

Unified Astronomy Thesaurus concepts: Astrophysical masers (103); Water masers (1790); Star formation (1569); Interstellar medium (847); Interstellar molecules (849); Stellar jets (1607); Protostars (1302); Jets (870)


1. Introduction

The star formation process is an important problem that astronomers have been addressing for decades. The process is especially problematic in the case of high-mass stars ($M_* \gtrsim 8 M_\odot$; Crowther et al. 2010) owing to their short lifetime and consequent scarcity of nearby objects and their frequent shrouding by interstellar material—so they are not easy to observe directly at short wavelengths, i.e., visible light—and because core nuclear fusion begins before the mass accretion process is complete. In order to observe inside the clouds, astronomers use a special technique of radio astronomy, very long baseline interferometry (VLBI; Rogers 1976; Thompson et al. 2017), to achieve very high angular resolution. In this technique, data from two or more widely separated radio telescopes are recorded on memory units for subsequent correlation.

Radio astronomers use a unique tool, cosmic masers, to penetrate the optically obscured star-forming regions (SFRs). The word “maser” was originally an acronym (Microwave Amplification by Stimulated Emission of Radiation) for the microwave analog of the laser. Studying the physical properties of masers toward the SFRs helps us to understand the properties of their environment, such as morphology, molecular

abundance, density, dust and gas temperatures, and velocity fields.

The 22,235 MHz H₂O maser is a common type of cosmic maser and easily detected in two types of Galactic objects: the envelopes of red supergiant and asymptotic giant branch stars and the disks and outflows associated with young stellar objects (e.g., Gray 2012). One excellent example of an SFR of this type is W49 North (W49 N, or G043.16+0.01), which is a region inside the high-mass SFR W49 A. It is the most luminous and complex SFR with H₂O masers in our galaxy (Cheung et al. 1969; Burke et al. 1970). An H₂O maser parallax distance of $11.11^{+0.79}_{-0.69}$ kpc has been measured (Zhang et al. 2013). The continuum sources were first identified by Dreher et al. (1984), i.e., seven main distinct components in W49 N and two subcomponents, which were observed at 1.5 and 2 cm using the Karl G. Jansky Very Large Array (VLA).⁹ Those components (hereafter called regions) were A, B, C, D, F, and G. Dreher et al. (1984) defined two edge-brightened shells on the west side of the G region: the G1 and G2 sources. Using the VLA, De Pree et al. (2000) observed 7 mm radio continuum emission toward W49 N at 43.3 GHz with 0^{''}.3 resolution and found that the G2 source can be divided into three subsources, i.e., G2a, G2b, and G2c (see Figure 2 of De Pree et al. 2000). Extensive high-frequency and high-resolution imaging with the VLA and the Berkeley–Illinois–Maryland Association array was more recently completed and newly classified by De Pree et al. (2004), including a more refined set of definitions that

 Original content from this work may be used under the terms of the [Creative Commons Attribution 4.0 licence](https://creativecommons.org/licenses/by/4.0/). Any further distribution of this work must maintain attribution to the author(s) and the title of the work, journal citation and DOI.

⁹ <https://public.nrao.edu/telescopes/vla/>

subdivide the earlier designations of regions, with a further subdivision indicated by a lower-case letter following each subsource, for example G1s, G2a, G2b, and G2c and similarly for other regions. The 22 GHz H₂O maser emission in W49 N has been observed and discussed in many previous works (Gwinn et al. 1992; Mac Low & Elitzur 1992, and references therein). The masers are found closely associated with the G1/G2 sources and exhibit their strongest flux from these regions. Almost all works have proposed that the maser emission arises from an outflow centered near the G region. However, there were numerous H₂O maser flares toward this region. For example, Honma et al. (2004) used a 20 m single dish of the VLBI Exploration of Radio Astrometry (VERA¹⁰) to monitor the maximum phase of the outburst of H₂O masers during 2003 October and also VLBI observations with the VERA array near its maximum phase. They found that the strongest outburst was at the local standard of rest (LSR) velocity of -30.7 km s^{-1} and located on the arc-like structure that was found in a region between G2a and G1, indicating a possible connection of the outburst to the shock phenomenon. Besides lots of detections of flux variability on the H₂O masers in W49N (e.g., Boboltz et al. 1998; Liljeström & Gwinn 2000; Zhou et al. 2002), other powerful flaring events were reported for three maser spectral components at LSR velocities of -81 , -60 , and $+6 \text{ km s}^{-1}$ in 2017–2020 (Volvach et al. 2019a, 2020, 2019b). However, accurate positions for these flare components have not been determined using VLBI.

There are a few intensive studies on the proper motions of H₂O maser features, starting with Gwinn et al. (1992). They used five epochs of five-station VLBI observations during 1980–1982. Those five telescopes were the 37 m Haystack antenna in Westford, Massachusetts; the 43 m telescope of the National Radio Astronomy Observatory (NRAO) at Green Bank, West Virginia; one of the 25 m antennas of the VLA near Socorro, New Mexico; the Caltech 40 m telescope at Owens Valley; and either the 100 m telescope of the Max-Planck-Institut für Radioastronomie at Effelsberg, (then) West Germany, or the 26 m telescope at Onsala, Sweden. They found 105 H₂O maser features around the G region and also computed expansion and rotation models of the H₂O maser bipolar outflow. Another previous work (Zhang et al. 2013) used very high precision data, which were taken by the Very Long Baseline Array (VLBA)¹¹ to study the proper motion of H₂O masers toward W49 N over the period 2010 March to 2011 April. They found numerous maser spots that appeared at four or more epochs within 1 yr and then selected only 11 maser spots detected at all 12 epochs in the arc-like structure of the G2a source. The absolute proper motion of the reference maser spot was found to be $\mu_x = -4.49 \pm 0.13$ and $\mu_y = -6.42 \pm 0.12 \text{ mas yr}^{-1}$. They also fitted the data to models of expansion with and without rotation, which were based on the previous study by Gwinn et al. (1992).

In this work, we will report the flux variability and proper-motion studies of H₂O masers toward the W49 N SFR by using data from the KaVA,¹² which observed this source at three epochs within the period 2017 February–May. We have computed expansion and rotation models of the H₂O maser bipolar outflow with a method that is independent of that employed by Gwinn et al. (1992).

2. Observations and Data Analysis

2.1. Observations and Constructing the Image Cubes

Observations of the H₂O ($6_{1,6}-5_{2,3}$) line at 22.235080 GHz were carried out with KaVA, which consists of four 20 m antennas of VERA in Japan and three 21 m antennas of the Korean VLBI Network (KVN). The maximum baseline length of KaVA is 2270 km, providing the highest angular resolution of 1.2 mas. The pointing and phase-tracking center position of the target source, W49 N, was taken to be

$$\begin{aligned} \text{R.A.}(J2000) &= 19^{\text{h}}10^{\text{m}}13^{\text{s}}.41, \\ \text{decl.}(J2000) &= +09^{\circ}06'14''.3. \end{aligned}$$

We observed W49 N in three epochs, each of which consisted of a time from horizon to horizon of 4.5 hr on two consecutive days. In the day-of-the-year (doy) system, these epochs were 058–059, 102–103, and 130–131 in 2017. The net on-source time was $3.2 \text{ hr epoch}^{-1}$.

Left-handed circular polarization data were recorded on the hard disk devices at 1 Gbps. The total bandwidth of each session was $8 \times 32 \text{ MHz}$, and a spectral resolution for the 22 GHz maser line was set to be 31.25 kHz, which corresponded to a total velocity coverage and resolution of 430 and 0.42 km s^{-1} , respectively. We assigned only one of the 32 MHz spectral windows to the 22 GHz H₂O masers. The systemic velocity of W49 N is equal to $+10.0 \text{ km s}^{-1}$ (Cesaroni et al. 1988). To cover a velocity range as wide as $\pm 300 \text{ km s}^{-1}$, with respect to the systemic velocity, we shifted the central frequency by 26 MHz (350 km s^{-1}) in the observations of two consecutive days. We observed a nearby calibrator, DA406, for bandpass and delay calibration once every hour.

Correlation processing was carried out at the Korea–Japan Correlation Center in KASI, Korea. Calibration and synthesis imaging were performed using the NRAO Astronomical Image Processing System (AIPS) software package (Greisen 2003) in the standard manner. We calibrated bandpass and delay by using a nearby (in angular separation from the source) calibrator, DA406. Phase calibration was done using the strongest H₂O maser spot in the first epoch, and it was the same position for every epoch¹³ in W49 N by fringe fitting and self-calibration. We adopted the V_{LSR} of the strongest channel in every epoch for doing self-calibration; these had values in the range $[+0.81; +1.20] \text{ km s}^{-1}$.

In order to search for maser emission in W49 N that was extended both in space (i.e., $2'' \times 2''$ square) and in velocity ($\sim 600 \text{ km s}^{-1}$), we made VLBI images using the following procedure. First, we made coarse images of W49 N for the first sessions (doy of 058 and 059 in 2017). All of the spectral channels in the 32 MHz bandwidth were analyzed to search for maser emission with a field of view of 800 mas and a 0.2 mas pixel size (4096×4096 pixels). To cover the $2'' \times 2''$ region, the center position of each image cube was shifted by 800 mas. Because of the extremely strong maser emission of $>10^4 \text{ Jy}$, the image dynamic range was limited by the strong side lobes. In order to exclude these side lobes, we set a detection threshold of five times the rms noise in each channel to identify the real maser spots. Next, we made full images for all of the

¹⁰ <https://www.miz.nao.ac.jp/veraserver/>

¹¹ <https://science.nrao.edu/facilities/vlba>

¹² The KVN and VERA Array.

¹³ Here we refer to a spot and feature as an individual maser emission at a single spectral channel and a group of spots detected in more than five consecutive spectral channels at positions coincident within the beam size, respectively.

sessions in all of the channels but only around the selected positions of identified maser features in the first session (doy of 058 and 059). We regard spots as real for the purposes of further data analysis if they were detected at least in two consecutive sessions and were spatially coincident with each other within the beam size and spectrally coincident within the velocity width. Because there were plenty of H₂O maser spots and many image fields, we developed program-specific software in the form of simple Fortran and bash shell scripts (see Phetra et al. 2019). After that, we applied Python scripts to classify the maser features and record the proper motion obtained from those features. Feature classification and proper-motion calculations are discussed in more detail in Sections 2.2.1 and 2.2.2.

2.2. Data Analysis

2.2.1. How to Define Maser Features

We measured the peak flux of H₂O maser spots by using the Gaussian fitting technique from the SAD task in AIPS. The results will be reported in terms of the position offset in R.A. and decl. and the LSR velocities in each channel. The position of a feature is defined as a weighted mean of the positions over the channels in which its constituent spots are detected, with the weighting being equal to the corresponding channel flux density of that spot,

$$\bar{x}_w = \frac{\sum_{i=1}^n x_i S_i^2}{\sum_{i=1}^n S_i^2}, \quad (1)$$

where x_i is the measured value in each channel, either the offset coordinate position or the v_{LSR} ; S_i is the channel flux density; and n is the number of data (spots) in the same feature. The standard deviation on the mean is used for the error value in each parameter, which is defined by

$$\sigma_x = \sqrt{\frac{\sum_{i=1}^n (x_i - \bar{x}_w)^2}{n - 1}}. \quad (2)$$

2.2.2. The Proper-motion Calculation

In order to define the movement of a feature over all three epochs, we used the following process.

1. The reference position of a stable feature should have the same position offset in every epoch.
2. All features will be shifted with respect to the stable reference feature.
3. As explained in Section 2, all weighted LSR velocities for each moving feature should have the same range, and the standard deviation of velocities should be within 2.0 km s^{-1} (i.e., $0.4 \text{ km s}^{-1} \times 5$ consecutive channels).

Even though we had only three epochs of data, we compared two methods for calculating the proper-motion results, following linear and quadratic equations (see Appendixes A and B for the explanation of the equations), which were obtained from the KaVA observations. However, the results calculated from the linear equation were realistic, while just some features were found to conform with the quadratic

equation. Therefore, the linear relationship was applied and fitted with the angular displacement of features in both R.A. and decl. offset. In order to avoid systematic errors, all of the proper motions in each direction were averaged, and the result was subtracted from each feature again. After that, square-root values of the proper motion in both R.A. and decl. offset (μ_{abs}) can be summarized from the equation $\mu_{\text{abs}} (\text{mas}) = \sqrt{\mu_x^2 + \mu_y^2}$. The transverse velocities were the vector quantity that was calculated from the basic equation, $v_t (\text{km s}^{-1}) = 4.7 \mu d$, where μ is the proper motion (in units of arcseconds per year), and d is the distance to W49 N (we adopt the value of $\sim 11.1 \text{ kpc}$; see Zhang et al. 2013). Radial velocities were calculated from the ‘‘radio definition’’ nonrelativistic Doppler shift equation, $v_{\text{obs}} = c \times \left(\frac{f_{\text{rest}} - f_{\text{obs}}}{f_{\text{rest}}} \right)$, where v_{obs} is the observation velocity in kilometers per second; f_{obs} and f_{rest} are the observation and rest frequency, respectively; and c is the velocity of light in vacuum, $299,792 \text{ km s}^{-1}$. The transverse and radial velocities will be used in the modeling of the H₂O maser bipolar outflow.

2.3. Comparison of the Maser Positions of KaVA with the High-accuracy VLBA Data

Since this observation lacked external phase-referencing astrometry, we could not directly obtain the absolute positions of masers. In order to compare the position offsets of maser features from the KaVA with the high-accuracy data of the VLBA (particularly the previous work by Zhang et al. 2013), we have applied some basic techniques to overlay and compare both data sets. The main processes can be explained as follows.

1. From a total of 102 moving features from the KaVA data, we select from the same range of data sets as those from Zhang et al. (2013, private communication) a small subset of at least three or four features in various well-separated positions, e.g., in the north, east, west, and south directions.
2. We make sure that they are the same features in both data sets; that is, the V_{LSR} should be within $\pm 0.4 \text{ km s}^{-1}$ or equal to one channel of the spectral resolution of the KaVA.
3. We calculate the difference of the position offsets from both data sets. Note that the values should not be dramatically different from each other in R.A. and decl. offset. After that, we average them together to get the finalized value of the offset.

The position offsets will be applied and adopted as KaVA absolute positions (i.e., $\sim 10 \text{ mas}$ accuracy) before overlaying with another facility, e.g., VLBA.

3. Analysis of Results

3.1. Total-power Spectrum

The 22 GHz H₂O masers in W49 N were observed with the KaVA at three epochs, i.e., 2017 February 27–28, 2017 March 12–13, and 2017 May 10–11 (hereafter called the first, second, and third epoch, respectively). The LSR velocities were between -300 and $+300 \text{ km s}^{-1}$. The total-power spectrum in each epoch was measured using the POSSM task in AIPS and plotted as shown in Figure 1. Blue and red lines represent two data sets that covered the LSR velocities as mentioned in Section 2. The dotted vertical line refers to the systemic velocity of this source, which is $+10 \text{ km s}^{-1}$. We found that the

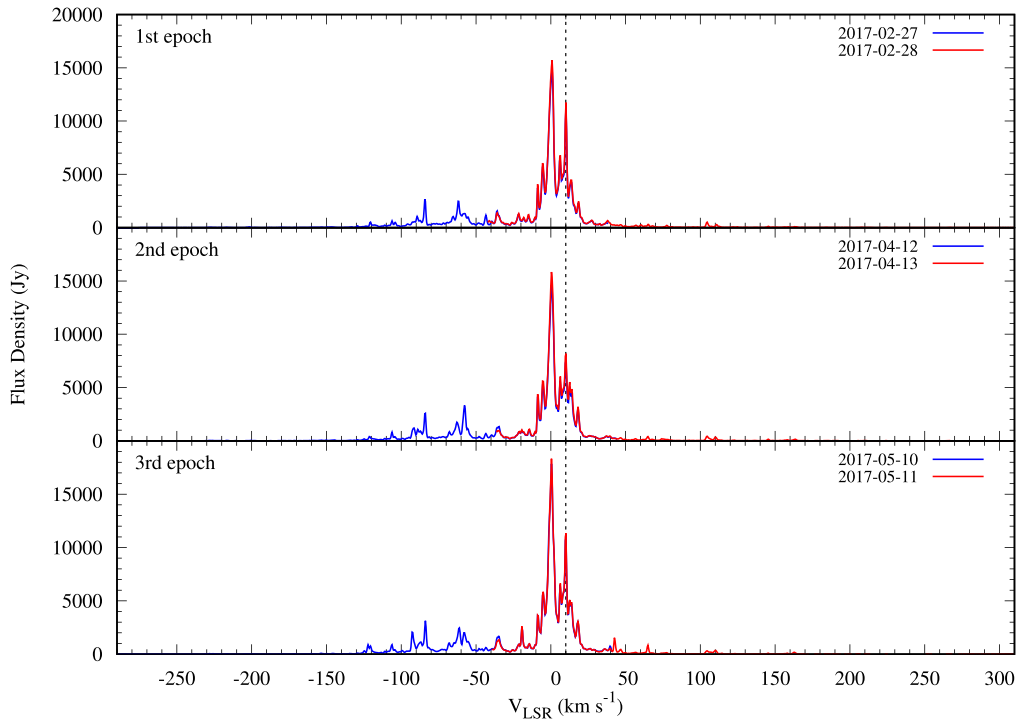


Figure 1. Total-power spectra of the 22 GHz H_2O maser emission toward W49 N from three epochs as seen by the KaVA. Blue and red lines represent two data sets that covered the LSR velocities. The dotted vertical line refers to the systemic velocity of this source ($+10.0 \text{ km s}^{-1}$). From top to bottom, the first, second, and third epoch are presented.

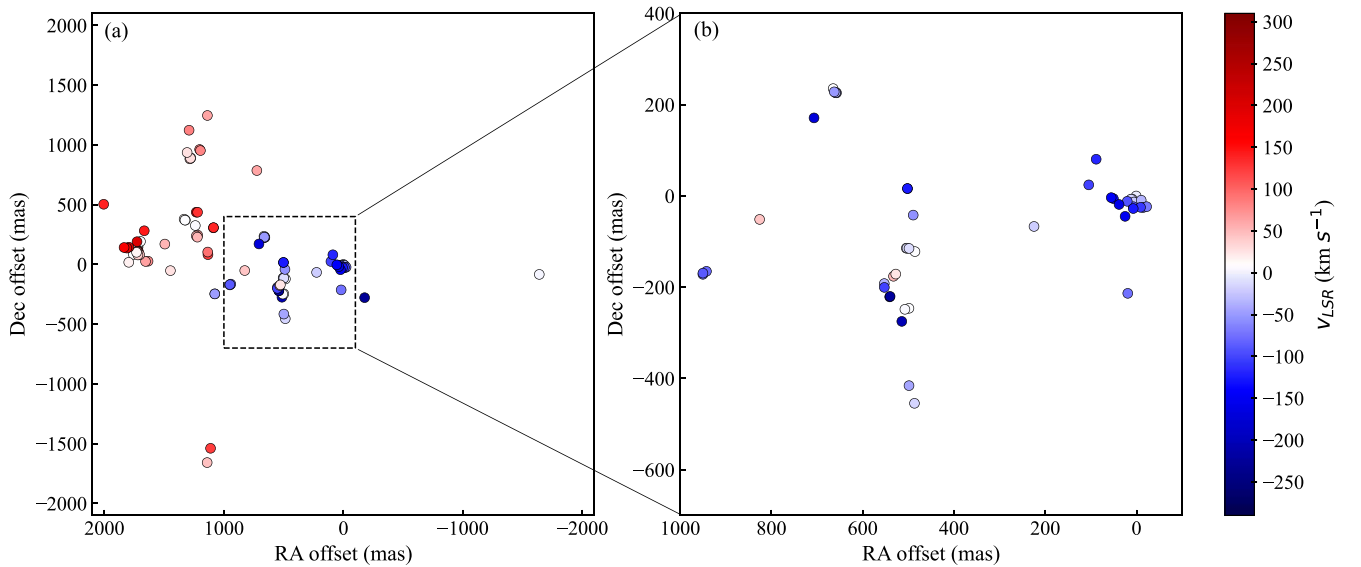


Figure 2. Panel (a) shows the distribution of 22 GHz H_2O maser features toward W49 N as observed by the KaVA. The features plotted are the subset that was found in all three epochs. The position offsets are relative to the strongest spots in each epoch, which are coincident (the same position within the beam size). The color bar on the right represents the LSR velocities (in units of kilometers per second). The arc-like structure in the vertical direction and the clumpy features that showed the strongest flux are inside the dashed box of panel (a) and magnified as shown in panel (b).

strongest flux was at $+0.47 \text{ km s}^{-1}$, and the highest flux density was $18,090 \text{ Jy}$ in 2017 May. Other high-flux spectral regions were within the highly blueshifted LSR velocity range $[-50:-100] \text{ km s}^{-1}$ in every epoch.

3.2. Number of Maser Features and Their Distribution

We determined the number of maser features using the criteria that are described in Section 2.2.1, and the number of features found in epochs 1–3 were 263, 268, and 310,

respectively. The number of features tended to increase, and we note especially that the third epoch has the highest number. These results are in good agreement with the previous work of Volvach et al. (2019a), in which they found significant flares of the 22 GHz H_2O maser emission during the period 2017 July to 2018 November. We plotted only the number of features that were found in all three epochs, as shown in panel (a) of Figure 2. Their distribution offsets are in a region of size $4 \times 4 \text{ arcsec}^2$. One maser feature is separated westward by $(-1.8,$

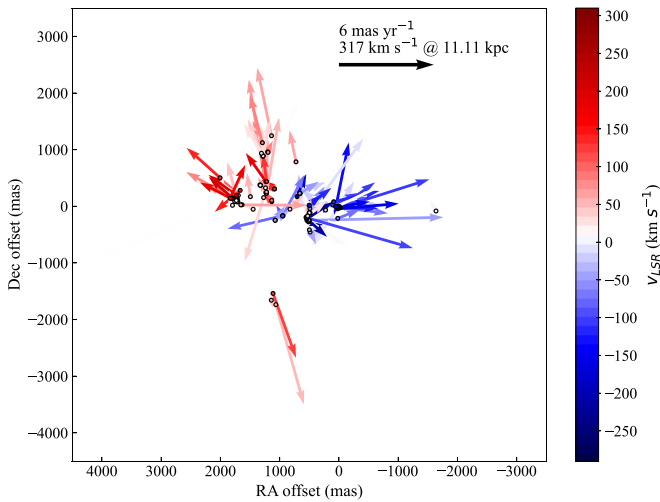


Figure 3. Proper motions of the 102 22 GHz water maser features that were detected by the KaVA at all three epochs. The length and direction of an arrow indicate the magnitude of the transverse velocity (given by the black arrow in the upper right corner of the panel) and its direction in R.A. and decl. offsets, respectively. The colors denote the epoch-averaged V_{LSR} range from -290 to $+310$ km s^{-1} of the maser features.

0.0) arcsec. The arc-like structure and the clumpy features that showed the strongest flux are marked inside the dashed box of panel (a) and magnified as shown in panel (b). Mostly, the redshifted and blueshifted LSR velocities were found in the eastern and western parts of the source, respectively.

3.3. The Internal Proper Motion

Figure 3 shows the proper motions of the subset of 22 GHz H_2O maser features that were detected by the KaVA at all three epochs. The length of each vector represents the magnitude of the proper motion compared to the standard (black arrow). The direction of each vector represents the direction of proper motion in R.A. and decl. offset coordinates. The colors of the arrows show the average radial velocity of each moving feature according to the color bar to the right of the figure. Only 102 features were classified as moving features over all three epochs (more details can be found in the Appendix D), and their weighted positions appear in Figure 2. The overall feature distribution is that of a red–blue divided shape, similar to a bipolar outflow, which is strong support to previous works, e.g., Gwinn et al. (1992) and Zhang et al. (2013). We mostly found that the features are moving outward (expansion) from their weighted mean positions. Predominantly blueshifted and redshifted velocities are found in the western and eastern parts of the source, respectively.

4. Discussion

In this discussion, we will focus on the following topics: (1) the location of the flux variable H_2O maser feature and (2) H_2O outflow modeling.

4.1. Location of the Flux Variable H_2O Maser Feature

The H_2O maser features at $V_{\text{LSR}} = -81, -60,$ and $+6$ km s^{-1} have been reported as exhibiting powerful flaring phenomena since 2017 (Volvach et al. 2019a, 2020, 2019b). These flares began in ~ 2017 September, ~ 2017 May, and ~ 2017 April, respectively. We conducted the KaVA

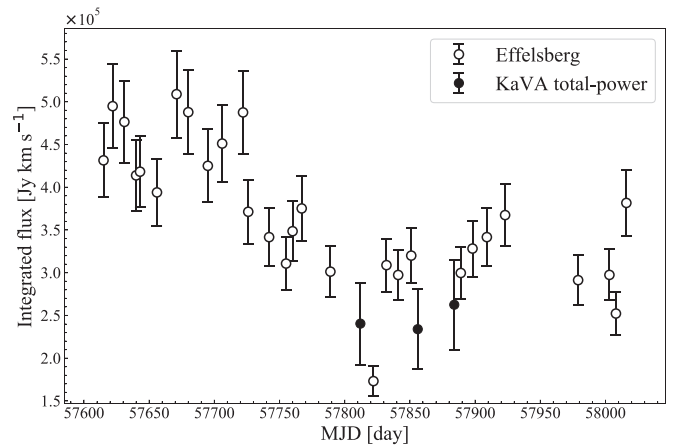


Figure 4. Variation plot for the integrated fluxes of the H_2O maser in W49 N from 2016 August to 2017 September. The flux observed with the Effelsberg 100 m radio telescope in Germany (B. H. Kramer et al. 2022 in preparation, and private communication) and the KaVA as total-power spectra in this paper is presented by white and black circles, respectively. These integrations were calculated over the LSR velocity range from -300 to $+300$ km s^{-1} . Error bars for integrated fluxes correspond to a typical value for scaling absolute flux of 10% and 20% in the Effelsberg and KaVA data, respectively.

monitoring observations in this paper on 2017 February 27–28, April 12–13, and May 10–11. The KaVA monitoring data thus potentially contribute to establishing the location of the feature responsible for the powerful H_2O maser flare at $V_{\text{LSR}} = +6$ km s^{-1} that began in ~ 2017 April. Indeed, the integrated fluxes of the KaVA total-power spectra, recorded in the LSR velocity range from -300 to $+300$ km s^{-1} , are among the weakest found during the period from 2016 August to 2017 September, as shown in Figure 4. In the figure, integrated fluxes in the same LSR velocity range observed with the Effelsberg 100 m radio telescope in Germany recorded in the period from 2016 August 15 (MJD 57,615) to 2017 September 20 (MJD 58,016) are also plotted (B. H. Kramer et al. 2022, in preparation, and private communication). These Effelsberg data enable us to clarify the trend of flare activity in this period, which decays until around early 2017 March (MJD $\sim 57,813$) and starts rebrightening during 2017 April–May. The rebrightening of the integrated flux until 2017 September is dominated by the powerful flares of the features at $V_{\text{LSR}} = -81$ and $+6$ km s^{-1} . The beginning of this rebrightening phase is coincident with the beginning of the flare at $V_{\text{LSR}} = +6$ km s^{-1} , determined in Volvach et al. (2019b), and the period of the KaVA observations in epochs 2 and 3.

Figure 5 shows a close-up of spatial distributions for the brightest channel at $V_{\text{LSR}} = +5.90$ km s^{-1} in H_2O maser feature 27 located at (x -offset, y -offset) $\sim (+507, -248)$ mas (see Tables 3 and 4) in epochs 1, 2, and 3. A peak maser spot in each epoch presented an intensity of 1920, 1973, and 2047 Jy beam^{-1} , respectively. Comparison of these intensities, taking into account an uncertainty in each absolute intensity value of 20%, suggests no clear flux variation in the spot based on VLBI maps in the KaVA observation period. We thus assume that this maser spot at $V_{\text{LSR}} = +5.90$ km s^{-1} could be identified as the one corresponding to the powerful flare feature at $V_{\text{LSR}} = +6$ km s^{-1} in Volvach et al. (2019b) on the basis of their coincidence of LSR velocities within the velocity resolution in the KaVA observations of 0.42 km s^{-1} . We cannot rule out the possibility of a maser–maser interaction scheme causing the powerful flares at $V_{\text{LSR}} = +6$ km s^{-1}

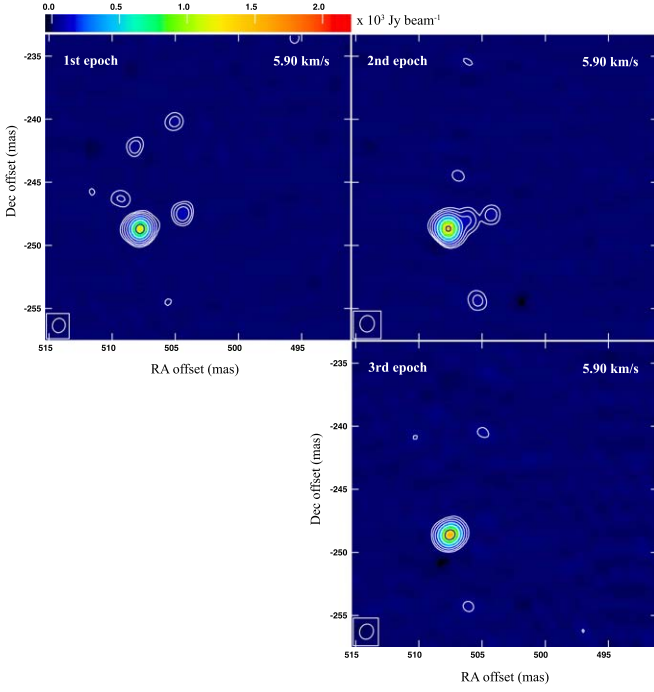


Figure 5. Close-up of a spatial distribution for the brightest channel at $V_{\text{LSR}} = +5.90 \text{ km s}^{-1}$ in H₂O maser feature 27 (see Tables 3 and 4); epochs 1, 2, and 3 are shown in the top left, top right, and bottom right panels, respectively. The position offsets are relative to the strongest spots in each epoch, which are coincident (the same position within the beam size). Synthesized beam sizes are indicated in the bottom left corner of each panel. Intensities are presented as colors with the color scale bar above the top left panel and white contours. Contour levels are 7, 14, 28, 56, 112, 224, ... times the rms noise levels of 2.22, 3.04, and 5.20 Jy beam⁻¹ in epochs 1, 2, and 3, respectively.

because of the pointlike structure of the spots in all three epochs. Sizes are 1.17×1.05 , 1.29×1.19 , and $1.29 \times 1.14 \text{ mas}^2$, comparable to the synthesized beam sizes of 1.14×1.01 , 1.30×1.14 , and $1.23 \times 1.07 \text{ mas}^2$, and prevent us from understanding whether multiple maser spots overlap along the line of sight. Furthermore, epochs 2 and 3 of the KaVA observations coincide with the earliest period of the initiation for the powerful flare. Nevertheless, we think it reasonable to claim that the powerful flare at $V_{\text{LSR}} = +6 \text{ km s}^{-1}$ could be excited by the shock front in the arc-like structured clump where the outburst at $V_{\text{LSR}} = -30.7 \text{ km s}^{-1}$ was detected in Honma et al. (2004), because this maser spot in the powerful flaring feature and the outbursting maser feature in Honma et al. (2004) coexist in a region of size $\sim 72 \text{ mas}$ in the arc-like structure, corresponding to $\sim 800 \text{ au}$ at the source distance.

4.2. Model Fits to the Data

We fitted a small number of models of the outflow structure to the data. These were, in increasing order of sophistication, a model in which the unknown z -position is computed from its 3D velocity and 2D sky position, models where the expansion velocity is described by single and double power laws, and a model where rotation of the bipolar structure is allowed in addition to a two-power expansion law. The theory for these models largely follows Equations (2)–(13) of Gwinn et al. (1992), but our analysis differs in a number of ways that are explained below. The first difference is in the method of solution that was used to determine the optimized values of the free parameters for each model. While Gwinn et al. (1992) used

a Levenberg–Marquardt method on N_p partial derivatives of the χ^2 statistic, where N_p is the number of free parameters, we used a combination of the simulated annealing and downhill simplex methods, implemented through the routines AMOTSA and AMOEBa (Press et al. 1997). This method has the advantage that only the χ^2 function itself needs to be computed, rather than the N_p derivatives. Another difference is that the z -offset velocity is treated as a free parameter in the most basic model by Gwinn et al. (1992), but we note that χ^2 is formally independent of this parameter in this model (see Appendix C). Notes on the individual models are listed below, and the results are summarized in Table 1.

1. Basic model. The χ^2 statistic is given by Equation (2) of Gwinn et al. (1992), which we show here as

$$\chi^2 = (3N_m - N_p)^{-1} \sum_{i=1}^{N_m} |\mathbf{u}_i - \mathbf{w}_i|^2, \quad (3)$$

where N_p is the number of free parameters to be fitted for by comparing observational velocities \mathbf{u}_i and model velocities \mathbf{w}_i for $i = 1 \dots N_m$ maser features, each supplying three components of the observed velocity vector, \mathbf{u}_i . The model velocities take the form $\mathbf{w}_i = \mathbf{v}_i + \mathbf{v}_0$, where \mathbf{v}_0 is a global velocity offset, and \mathbf{v}_i is the model-dependent flow velocity computed for the i th maser feature. The sole assumption about the flow velocity in this model, as in Equation (7) of Gwinn et al. (1992), is that it is radial in direction with respect to an offset position. Each feature can have an independent magnitude of the velocity. A consequence is that the source distance is indeterminate. A distance of 12.0 kpc was assumed to convert angular to linear distances in the sky plane.

The set of parameters, in principle, includes the three components of \mathbf{v}_0 ; the two sky components, x_0 and y_0 , of the offset position; and the z -position of every maser feature. However, by taking a partial derivative of Equation (3) with respect to z_i , the z -position of feature i , it is possible to show that the unknown z -positions may be determined analytically from the five remaining independent parameters from the equation

$$z_i = \frac{(u_{iz} - v_{0z})[(x_i - x_0)^2 + (y_i - y_0)^2]}{(u_{ix} - v_{0x})(x_i - x_0) + (u_{iy} - v_{0y})(y_i - y_0)}. \quad (4)$$

This is a corrected version of Equation (8) of Gwinn et al., noting that the original is dimensionally incorrect. We go on to show in Appendix C that the final model velocity \mathbf{w}_i of each feature is also independent of v_{0z} , so this model ends up with four independent parameters: the x - and y -components of the position and velocity offsets from the reference position and velocity, respectively.

2. Single power law. In this and all later models, χ^2 follows from Equation (10) of Gwinn et al. We reproduce the equation here in the form

$$\chi^2 = (3N_m - N_p)^{-1} \sum_{i=1}^{N_m} \left\{ \frac{[u_{xi} - (d_0/d)w_{xi}]^2}{\sigma_{xi}^2} + \frac{[u_{yi} - (d_0/d)w_{yi}]^2}{\sigma_{yi}^2} + \frac{[u_{zi} - w_{zi}]^2}{\sigma_{zi}^2} \right\}. \quad (5)$$

The observational velocities now have an associated measurement error σ_i . Comparing Equation (5) with

Table 1
Fitting Parameters of Models Applied to the KaVA Data

Parameter	Units	Model 1	Model 2	Model 3	Model 4
x -offset	arcsec	1.34 ± 0.30	0.16 ± 0.18	0.38 ± 0.08	0.22 ± 0.07
y -offset	arcsec	-0.33 ± 0.08	-0.77 ± 0.19	-0.25 ± 0.17	-0.38 ± 0.25
v_x -offset	km s^{-1}	37.19 ± 26.15	-43.24 ± 6.41	-43.31 ± 5.12	-43.49 ± 4.55
v_y -offset	km s^{-1}	-34.03 ± 7.84	-45.41 ± 10.74	-24.70 ± 8.44	-32.09 ± 15.15
v_z -offset	km s^{-1}	...	-12.17 ± 13.36	-22.73 ± 20.77	-13.90 ± 12.66
Distance	kpc	...	10.68 ± 1.47	11.12 ± 0.99	11.12 ± 0.96
V_0	$\text{km s}^{-1} \text{ arcsec}^{-\alpha_0}$...	16.10 ± 4.79	17.58 ± 5.29	17.33 ± 6.29
α_0	2.78 ± 0.40	0.07 ± 0.77	1.68 ± 0.97
V_1	$\text{km s}^{-1} \text{ arcsec}^{-\alpha_1}$	20.85 ± 5.72	8.23 ± 5.37
α_1	3.00 ± 0.68	3.20 ± 0.56
ω_x	$\text{km s}^{-1} \text{ arcsec}^{-(\gamma+1)}$	-8.24 ± 3.92
ω_y	$\text{km s}^{-1} \text{ arcsec}^{-(\gamma+1)}$	7.20 ± 3.39
ω_z	$\text{km s}^{-1} \text{ arcsec}^{-(\gamma+1)}$	3.82 ± 3.35
γ	-0.18 ± 0.57
χ^2	...	1275^a	7.91	8.02	7.82

Note.

^a In $(\text{km s}^{-1})^2$, χ^2 is dimensionless in all other models. Model 1 has an assumed distance of 12.0 kpc.

Table 2
Comparison of the Distance Measurements toward W49 N from Previous Works and the Current Study

Reference	Method	Distance (kpc)	Telescope/Facility
Mezger et al. (1967)	Radio continuum and recombination line Emission at frequency ranges 195 MHz to 15.4 GHz	14.1	See remark ^a
Gwinn et al. (1992)	Proper motions of H ₂ O maser	11.4 ± 1.2	See remark ^b
Zhang et al. (2013)	Trigonometric parallax of H ₂ O maser	$11.11^{+0.79}_{-0.69}$	VLBA
Current study	Proper motions of H ₂ O maser	11.12 ± 0.99 11.12 ± 0.96	KaVA [model 3] KaVA [model 4]

Notes.

^a The Mullard Observatory, Cambridge, England; the Arecibo Ionospheric Observatory 1000 foot telescope; the NRAO 300 foot telescope; the NRAO 140 foot telescope; and the Haystack 120 foot telescope.

^b Five-station global VLBI; for the list of stations, see Section 1.

Equation (3), there is now a distinction between the distance-independent velocity measurements in the z -component and the distance-dependent motions in the sky plane, making the source distance a free parameter. This is written in the dimensionless form d/d_0 , where the scaling distance $d_0 = 12.0$ kpc. Flow velocities now have an assumed functional form for each model (N) with $N > 1$. In this case, model 2, the flow velocity is given by

$$v_i = \hat{r}_i V_0 r_i^{\alpha_0}, \quad (6)$$

where $\mathbf{r}_i = [(x_i - x_0), (y_i - y_0), z_i]$, and r_i is the magnitude of this vector. The expression \hat{r}_i is the unit form of \mathbf{r}_i . Equation (6) adds four fitting parameters: the sky position offsets x_0 and y_0 , the bulk flow constant V_0 , and the expansion power law α_0 . The dimensions of V_0 are fixed by the requirement that the expression $V_0 r_i^{\alpha_0}$ must be a velocity. The single power-law case was not explicitly investigated by Gwinn et al. (1992) but follows from their Equation (11) by the simple expedient of setting $V_1 = 0$. A solution for this model is computed in Zhang et al. (2013). There are eight free parameters after elimination of the z -positions: the two sky position offsets, three velocity offsets, the distance, V_0 , and α_0 .

As in model 1, we may take a partial derivative of the formula for χ^2 , in this case, Equation (5), with respect to a z -position, z_j . The resulting expression still allows the

elimination of the z -positions in terms of the eight free parameters listed above. However, unlike Equation (4), the equation is nonlinear and must be solved numerically. A similar scheme applies to models 3 and 4 below.

3. Double power law. This follows model 2 of Gwinn et al. The flow velocities are now computed from

$$v_i = \hat{r}_i (V_0 r_i^{\alpha_0} + V_1 r_i^{\alpha_1}), \quad (7)$$

which is designed to better fit an expansion with a fast and a slow component. Equation (7) adds two additional fitting parameters compared with Equation (6), so there are now 10 free parameters after elimination of the z -positions, and this model offers the best possibility for a direct comparison of the solution methods by substituting the KaVA data with the data from Table 4 of Gwinn et al. (1992).

4. Double power law with rotation. This model has the same structure as model 4 of Gwinn et al. (their Table 5). The flow velocity is now represented as

$$v_i = \hat{r}_i (V_0 r_i^{\alpha_0} + V_1 r_i^{\alpha_1}) + r_i^\gamma \boldsymbol{\omega} \times \mathbf{r}_i, \quad (8)$$

where the group $r_i^\gamma \boldsymbol{\omega}$ has the dimensions of an angular velocity and represents rotation of the outflow axis. The rotational term introduces a radial dependence, controlled by the index γ and a direction, represented by $\boldsymbol{\omega}$, so there are four additional free parameters compared with model

3, bringing the total to 14 after elimination of the z -positions.

The uncertainty estimates on the model parameters in Table 1 were determined by running the model from different starting positions; the uncertainty is the sample standard deviation of 10 trials for each model. The results for our models are not completely in accord with those of either Gwinn et al. (1992) or Zhang et al. (2013). The most important difference is in the velocity offset. However, the most important parameter, the source distance, is reasonably robust in the more sophisticated models that include an adequate number of fitting parameters. The value 11.12 ± 0.96 kpc from our model 4 is consistent with the value of $11.11_{-0.69}^{+0.79}$ kpc derived from parallax by Zhang et al. (2013). The distance estimate from our model 2, though less accurate, is also consistent with the parallax distance (see comparison of the distance measurements toward W49 N from previous works and the current study in Table 2). Our model with rotation is consistent with a radial power of $\gamma = 0.0$, which makes our model closest to model 3 of Gwinn et al. in this respect. Our fits to the components of the rotation vector are consistent with those of model 3 of Gwinn et al., so its orientation with respect to the axis of the maser outflow looks the same within the errors as in Figure 8 of Gwinn et al. (1992).

4.3. Tests of the Algorithm

The optimization algorithm containing the AMOTSA and AMOEBa codes from Press et al. (1997) was tested on a generic function not related to the present work. The function is the D -dimensional multispikes function,

$$f(x_1, x_2, x_3 \dots x_D) = 1 - \left\{ 4^D \prod_{i=1}^D x_i (1 - x_i) \sin(n\pi x_i) \right\}^2, \quad (9)$$

which is used because it contains a large number of local minima controlled by the parameter n and a global minimum at $x_i = 0.5$ for all $1 \leq i \leq D$. It is therefore a challenging problem to identify the global minimum among all of its close rivals.

For the case where $n = 21$ and $D = 4$, the same as in model 1, the algorithm was able to detect the global minimum to an accuracy of 0.01 after 10 attempts, starting from different random points in the 4D unit volume. The algorithm was allowed a total of 10^8 moves, with 10^5 at any one of 1000 ‘‘temperatures.’’ The stiffness factor that controls the number of high temperatures relative to the number of low temperatures was set to 1.2.

5. Conclusion

We have studied the proper motions of 22 GHz H₂O masers toward the W49 N region using the KaVA over three epochs during 2017 February to May. The main results of this study are as follows.

1. The H₂O maser features were distributed in a region of 4×4 arcsec² or 0.30×0.30 pc², and the highest flux density was 18,090 Jy. They also show a bipolar outflow structure with wide-angle wind morphology in the northeast direction and an inclination angle of $37^\circ \pm 13^\circ$ to the line of sight.

2. The averaged internal proper motions in the R.A. and decl. offsets were -0.352 and $+0.890$ mas yr⁻¹, respectively.
3. On the basis of VLBI maps with the KaVA catching the timing at just before and during the rebrightening phase, the powerful flaring H₂O maser feature at $+6$ km s⁻¹ is possibly located at (x -offset, y -offset), i.e., $\sim (+507, -248)$ mas (see Tables 3 and 4 in Appendix D) from the LSR velocity correspondence basis and could be excited by the shock front in the arc-like structured clump, where the outburst was detected by Honma et al. (2004), i.e., VLSR = -30.7 km s⁻¹, although the possibility of a maser–maser interaction scheme could not be ruled out due to the pointlike spatial structures of the maser spots in all three VLBI epochs.
4. Modeling of the H₂O masers as an expanding region with rotation yields a distance to W49 N of 11.12 ± 0.96 kpc. This value is consistent with the value recovered from trigonometric parallax observations of masers in Zhang et al. (2013) and earlier modeling results from Gwinn et al. (1992).

K.A. would like to thank NARIT and Thailand Science Research and Innovation (TSRI) for supporting budget No. 13/FY2563 and grant No. MRG5580019 during the Thai fiscal year 2015–2019; also, some budgets were supported by Khon Kaen University, Thailand. K.A. also thanks T. Chanapote for helping in the plots and solving equations. M.D.G. would like to thank the University of Manchester and NARIT for funding during his sabbatical year in Chiang Mai, 2019–2020. T.H. is financially supported by MEXT/JSPS KAKENHI grant Nos. 17K05398, 18H05222, and 20H05845.

Facility: KaVA.

Software: AIPS (Greisen 2003).

Appendix A Analysis of the Proper Motion

To analyze the proper motion, we need to consider a suitable equation for calculating the displacement angle in both R.A. and decl. offset. Even though the time range of observations was rather short, a total of 72 days, we have still considered two types of evolution equations: quadratic and linear.

A.1. Quadratic Equation

The basic evolution equation of the quadratic system is

$$x = at^2 + bt + c, \quad (A1)$$

where x is the position offset (R.A. and decl. in units of milliarcseconds), t is the day of the year 2017, and a , b , and c are the unknown parameters, or coefficients.

In the present work, there are three epochs, and the solutions for each feature are as follows:

$$x_1 + \Delta x_1 = at_1^2 + bt_1 + c, \quad (A2)$$

$$x_2 + \Delta x_2 = at_2^2 + bt_2 + c, \quad (A3)$$

$$x_3 + \Delta x_3 = at_3^2 + bt_3 + c, \quad (A4)$$

where x_1 , x_2 , and x_3 are the position offset of each epoch, and t_1 , t_2 , and t_3 are the day of each epoch. The matrix form of

Equation (A2) is

$$\begin{pmatrix} t_1^2 & t_1 & 1 \\ t_2^2 & t_2 & 1 \\ t_3^2 & t_3 & 1 \end{pmatrix} \begin{pmatrix} a \\ b \\ c \end{pmatrix} = \begin{pmatrix} x_1 + \Delta x_1 \\ x_2 + \Delta x_2 \\ x_3 + \Delta x_3 \end{pmatrix}. \quad (\text{A5})$$

We used Cramer's rule to calculate the unknown parameters. The solutions are

$$a = \frac{D_a}{D}, \quad b = \frac{D_b}{D}, \quad c = \frac{D_c}{D}, \quad (\text{A6})$$

where

$$D = \det \begin{vmatrix} t_1^2 & t_1 & 1 \\ t_2^2 & t_2 & 1 \\ t_3^2 & t_3 & 1 \end{vmatrix}, \quad D_a = \det \begin{vmatrix} (x_1 + \Delta x_1) & t_1 & 1 \\ (x_2 + \Delta x_2) & t_2 & 1 \\ (x_3 + \Delta x_3) & t_3 & 1 \end{vmatrix}, \quad (\text{A7})$$

$$D_b = \det \begin{vmatrix} t_1^2 & (x_1 + \Delta x_1) & 1 \\ t_2^2 & (x_2 + \Delta x_2) & 1 \\ t_3^2 & (x_3 + \Delta x_3) & 1 \end{vmatrix}, \quad D_c = \det \begin{vmatrix} t_1^2 & t_1 & (x_1 + \Delta x_1) \\ t_2^2 & t_2 & (x_2 + \Delta x_2) \\ t_3^2 & t_3 & (x_3 + \Delta x_3) \end{vmatrix}, \quad (\text{A8})$$

or

$$D = t_1^2 t_2 + t_3^2 t_1 + t_2^2 t_3 - t_3^2 t_2 - t_1^2 t_3 - t_2^2 t_1, \quad (\text{A9})$$

$$\begin{aligned} D_a &= (x_1 + \Delta x_1)t_2 + (x_3 + \Delta x_3)t_1 + (x_2 + \Delta x_2)t_3 \\ &\quad - (x_3 + \Delta x_3)t_2 - (x_1 + \Delta x_1)t_3 - (x_2 + \Delta x_2)t_1 \\ &= (x_1 t_2 + x_3 t_1 + x_2 t_3 - x_3 t_2 - x_1 t_3 - x_2 t_1) \\ &\quad + (\Delta x_1 t_2 + \Delta x_3 t_1 + \Delta x_2 t_3 - \Delta x_3 t_2 - \Delta x_1 t_3 - \Delta x_2 t_1) \\ &= D_{a,0} + \Delta D_a, \end{aligned} \quad (\text{A10})$$

$$\begin{aligned} D_b &= t_1^2(x_2 + \Delta x_2) + t_3^2(x_1 + \Delta x_1) + t_2^2(x_3 + \Delta x_3) \\ &\quad - t_3^2(x_2 + \Delta x_2) - t_1^2(x_3 + \Delta x_3) - t_2^2(x_1 + \Delta x_1) \\ &= (t_1^2 x_2 + t_3^2 x_1 + t_2^2 x_3 - t_3^2 x_2 - t_1^2 x_3 - t_2^2 x_1) \\ &\quad + (t_1^2 \Delta x_2 + t_3^2 \Delta x_1 + t_2^2 \Delta x_3 - t_3^2 \Delta x_2 - t_1^2 \Delta x_3 - t_2^2 \Delta x_1) \\ &= D_{b,0} + \Delta D_b, \end{aligned} \quad (\text{A11})$$

$$\begin{aligned} D_c &= t_1^2 t_2(x_3 + \Delta x_3) + t_3^2 t_1(x_2 + \Delta x_2) + t_2^2 t_3(x_1 + \Delta x_1) \\ &\quad - t_3^2 t_2(x_1 + \Delta x_1) - t_1^2 t_3(x_2 + \Delta x_2) - t_2^2 t_1(x_3 + \Delta x_3) \\ &= (t_1^2 t_2 x_3 + t_3^2 t_1 x_2 + t_2^2 t_3 x_1 - t_3^2 t_2 x_1 - t_1^2 t_3 x_2 - t_2^2 t_1 x_3) \\ &\quad + (t_1^2 t_2 \Delta x_3 + t_3^2 t_1 \Delta x_2 + t_2^2 t_3 \Delta x_1 - t_3^2 t_2 \Delta x_1 - t_1^2 t_3 \Delta x_2 - t_2^2 t_1 \Delta x_3) \\ &= D_{c,0} + \Delta D_c. \end{aligned} \quad (\text{A12})$$

Then, the unknown parameters are

$$a = \frac{D_a}{D} = \frac{D_{a,0}}{D} + \frac{\Delta D_a}{D} = a_0 + \Delta a, \quad (\text{A13})$$

$$b = \frac{D_b}{D} = \frac{D_{b,0}}{D} + \frac{\Delta D_b}{D} = b_0 + \Delta b, \quad (\text{A14})$$

$$c = \frac{D_c}{D} = \frac{D_{c,0}}{D} + \frac{\Delta D_c}{D} = c_0 + \Delta c. \quad (\text{A15})$$

Finally, the proper motion at epoch i is the slope from Equation (A1) as follows:

$$\begin{aligned} m_{i,Q} &= \left. \frac{dx}{dt} \right|_{t=t_i} \\ &= 2at_i + b \end{aligned} \quad (\text{A16})$$

$$\begin{aligned} &= 2(a_0 + \Delta a)t_i + (b_0 + \Delta b) \\ &= \mu_{i,Q} + \Delta \mu_{i,Q}, \end{aligned} \quad (\text{A17})$$

and the units of m_i are milliarcseconds per day.

Appendix B Linear Equation

The main evolution equation of the linear system is

$$x = dt + e, \quad (\text{B1})$$

where d and e are the unknown parameters. The solutions for calculation of the unknown parameters are

$$d = \frac{\sum_{i=1}^n x_i t_i - n \bar{x} \bar{t}}{\sum_{i=1}^n t_i^2 - n \bar{t}^2}, \quad (\text{B2})$$

$$e = \bar{x} - d \bar{t}. \quad (\text{B3})$$

For observed data $x + \Delta x$, the average values in normal form are $\bar{x} + \Delta \bar{x}$. Then, the final forms of d and e are

$$d = \frac{\sum_{i=1}^n (x_i + \Delta x) t_i - n(\bar{x} + \Delta \bar{x}) \bar{t}}{\sum_{i=1}^n t_i^2 - n \bar{t}^2} \quad (\text{B4})$$

$$= \frac{\sum_{i=1}^n x_i t_i - n \bar{x} \bar{t}}{\sum_{i=1}^n t_i^2 - n \bar{t}^2} + \frac{\sum_{i=1}^n \Delta x_i t_i - n \Delta \bar{x} \bar{t}}{\sum_{i=1}^n t_i^2 - n \bar{t}^2} \quad (\text{B5})$$

$$= d_0 + \Delta d,$$

$$\begin{aligned} e &= (\bar{x} + \Delta \bar{x}) - (d_0 + \Delta d) \bar{t} \\ &= (\bar{x} - d_0 \bar{t}) + (\Delta \bar{x} - \Delta d \bar{t}) \\ &= e_0 + \Delta e. \end{aligned} \quad (\text{B6})$$

Finally, the proper motion is the slope from Equation (B1) as follows:

$$m_i = d, \quad (\text{B7})$$

$$= d_0 + \Delta d, \quad (\text{B8})$$

$$= \mu_i + \Delta \mu_i, \quad (\text{B9})$$

where the units of m_i are milliarcseconds per day.

Appendix C Proof that v_{0z} is Redundant in Model 1

We begin with Equation (4) of the main text, a formula for the unknown z -position of the i th maser feature, where each feature has a measured velocity vector (u_{ix} , u_{iy} , u_{iz}) and a measured sky position (x_i , y_i), and the model has a velocity offset (u_{0x} , u_{0y} , u_{0z}) and sky position offset (x_0 , y_0). Equation (4) is essentially Equation (8) of Gwinn et al. (1992) but with the position offsets included and the dimensions corrected. We simplify Equation (4) by defining the 2D radius $\boldsymbol{\rho} = ((x_i - x_0), (y_i - y_0))$, and the 2D dot product,

$$\begin{aligned} \mathbf{q}_i \cdot \boldsymbol{\rho}_i &= (u_{ix} - v_{0x})(x_i - x_0) \\ &\quad + (u_{iy} - v_{0y})(y_i - y_0), \end{aligned} \quad (\text{C1})$$

noting that \mathbf{q}_i is the sky plane velocity relative to its component offsets. The simplified form is therefore

$$z_i = (u_{iz} - v_{0z}) \rho_i^2 / \mathbf{q}_i \cdot \boldsymbol{\rho}_i. \quad (\text{C2})$$

We ultimately seek to show that components of the model velocity $\mathbf{w}_i = \mathbf{v}_0 + \mathbf{v}_i$ (see Equation (4) of Gwinn et al. 1992) are all independent of v_{0z} , since Equation (2) of Gwinn et al. contains only the \mathbf{w}_i and measured velocities. It is useful to take Equation (5) of Gwinn et al. (1992) with $p_j = V_0(j)$, the

flow velocity of a particular maser feature. As these velocities are individual to each feature, the sum over the features collapses, and the problem reduces to evaluating partial differentials of the form $\partial v_i / \partial V_0(i)$. From the definition of the flow velocity (Equation (7) of Gwinn et al. 1992), these differentials reduce to \mathbf{r}_i / r_i , and Equation (5) of that work becomes the dot product,

$$(\mathbf{u}_i - \mathbf{w}_i) \cdot \mathbf{r}_i = 0. \quad (\text{C3})$$

This equation does not appear explicitly in Gwinn et al. (1992) but is alluded to in the text following their Equation (9). A more useful version of Equation (C3) is obtained by expanding \mathbf{w}_i in terms of v_{0i} and v_i and further expanding v_i as a flow velocity from Equation (5) of Gwinn et al. (1992). With the flow speed as the subject,

$$V_0(i) = [(\mathbf{u}_i - \mathbf{v}_0) \cdot \mathbf{r}_i] / r_i. \quad (\text{C4})$$

It is useful to divide Equation (C4) by r_i before expanding the dot product and eliminating all occurrences of z_i with the aid of Equation (C2), yielding

$$\frac{V_0(i)}{r_i} = \frac{(u_{ix} - v_{0x})(x_i - x_0) + (u_{iy} - v_{0y})(y_i - y_0) + (u_{iz} - v_{0z})^2 \rho_i^2 / (\mathbf{q}_i \cdot \boldsymbol{\rho}_i)}{(x_i - x_0)^2 + (y_i - y_0)^2 + (u_{iz} - v_{0z})^2 \rho_i^4 / (\mathbf{q}_i \cdot \boldsymbol{\rho}_i)^2}, \quad (\text{C5})$$

where we have used $r_i^2 = \rho_i^2 + z_i^2$ for the squared magnitude of the 3D position. After identification of the 2D dot product in the numerator and ρ_i^2 in the denominator, a cancellation is

possible, and Equation (C5) reduces to

$$\frac{V_0(i)}{r_i} = \frac{\mathbf{q}_i \cdot \boldsymbol{\rho}_i}{\rho_i^2}, \quad (\text{C6})$$

which is obviously independent of v_{0z} because the vectors \mathbf{q}_i and $\boldsymbol{\rho}_i$ are both 2D sky plane quantities.

To complete the proof, we note that the x -component of the flow velocity is $v_{ix} = V_0(i)(x_i - x_0) / r_i$ from Equations (3), (4), and (7) of Gwinn et al. (1992). The right-hand side of this expression is the right-hand side of Equation (C6) multiplied by a relative x -position, neither of which contain v_{0z} . To form the model x -velocity, w_{ix} , we add only v_{0x} , so this model velocity component is also independent of v_{0z} . A very similar argument holds for the model y -velocity. The z -component is slightly different; we begin in the same way with

$$v_{iz} = V_0(i)z_i / r_i = z_i(\mathbf{q}_i \cdot \boldsymbol{\rho}_i) / \rho_i^2, \quad (\text{C7})$$

but it is then best to eliminate the dot product and the factor of $1/\rho_i^2$ with the aid of Equation (C2), leaving, simply, $v_{iz} = u_{iz} - v_{0z}$. In this case, the flow velocity does depend on v_{0z} , but upon adding v_{0z} to generate w_{iz} , this dependence is lost. We have now demonstrated that all three components of \mathbf{w}_i are independent of v_{0z} and so, therefore, is the χ^2 , or S^2 , statistic, given by Equation (2) of Gwinn et al. (1992).

Appendix D

Results from the Proper-motion Analysis

These tables show the results obtained from the proper-motion analysis according to the quadratic and linear fitting (Tables 3 and 4).

Table 3
Proper Motion of H₂O Maser Features Calculated from Quadratic Fitting

Fea. No.	x -offset ^a (mas)	δx^b (mas)	y -offset ^c (mas)	δy (mas)	μ_x^d (mas yr ⁻¹)	$\delta \mu_x^{+e}$ (mas yr ⁻¹)	$\delta \mu_x^{-f}$ (mas yr ⁻¹)	μ_y^g (mas yr ⁻¹)	$\delta \mu_y^{+h}$ (mas yr ⁻¹)	$\delta \mu_y^{-i}$ (mas yr ⁻¹)	V_{LSR}^h (km s ⁻¹)	δV_{LSR}^i (km s ⁻¹)
1	-1638.531	0.089	-83.855	0.032	1.319	1.758	-2.976	-0.516	2.154	0.000	5.06	0.31
2	19.138	0.003	-213.446	0.005	-2.563	0.000	-0.81	-1.839	1.586	0.000	-74	0.23
3	0.690	0.050	-0.156	0.018	1.124	0.874	-2.092	-1.29	1.908	0.000	0.38	0.21
4	9.409	0.023	-6.941	0.025	0.687	0.213	-1.431	-1.687	2.300	0.000	-4.78	0.05
5	12.045	0.010	-7.016	0.093	-1.127	0.132	-1.35	-0.851	4.464	-1.752	-13.68	0.13
6	5.576	0.009	-13.332	0.002	-1.624	0.000	-1.008	-0.228	1.737	0.000	-21.94	0.21
7	-10.302	0.011	-9.319	0.007	-5.284	0.232	-1.449	5.463	2.236	0.000	-32.55	0.26
8	-14.523	0.043	-25.361	0.022	-0.086	0.590	-1.808	-5.532	1.997	0.000	-63.56	1.32
9	-22.183	0.066	-23.541	0.010	-10.075	1.503	-2.721	-0.152	1.729	0.000	-69.05	1.07
10	6.952	0.022	-23.63	0.014	-3.968	0.027	-1.244	-0.239	1.774	0.000	-86.27	0.12
11	20.247	0.011	-11.813	0.009	-0.359	0.000	-0.941	-3.276	1.639	0.000	-91.72	0.24
12	-5.678	0.026	-27.289	0.015	-8.465	1.248	-2.466	3.679	2.711	0.000	-104.93	0.92
13	-8.905	0.039	-24.94	0.055	-4.105	0.620	-1.838	-2.499	3.185	-0.473	-106.83	0.20
14	7.147	0.020	-27.615	0.024	-1.241	0.000	-1.207	-2.94	2.059	0.000	-123.66	0.48
15	50.641	0.349	-5.896	0.757	-1.568	10.790	-12.008	-2.311	27.672	-24.96	-134.28	0.99
16	24.975	0.297	-44.737	0.301	0.499	8.143	-9.361	-1.877	9.168	-6.456	-153.24	0.55
17	38.237	0.013	-18.7	0.016	-6.932	0.000	-1.18	0.023	1.892	0.000	-159.15	0.17
18	104.643	0.062	24.230	0.162	-4.287	1.721	-2.939	-2.119	5.851	-3.138	-100.96	0.59
19	55.385	0.243	-3.712	0.180	4.739	5.850	-7.068	-2.337	6.390	-3.678	-145.42	0.23
20	88.388	0.188	80.431	0.031	1.307	4.950	-6.168	-0.506	2.338	0.000	-118.02	0.56
21	224.568	0.080	-66.88	0.025	1.532	1.683	-2.9	-0.334	2.086	0.000	-19.55	0.50
22	486.535	0.003	-454.412	0.005	-0.727	0.000	-0.718	-1.63	1.547	0.000	-13.63	0.38
23	498.497	0.015	-415.696	0.022	-0.789	0.000	-1.214	-2.425	2.153	0.000	-43.19	0.19
24	538.492	0.263	-250.292	0.321	-18.516	6.798	-8.015	-3.358	8.291	-5.578	-47.33	0.52
25	514.292	0.136	-274.89	0.032	-0.011	3.391	-4.608	-1.076	2.350	0.000	-201.07	0.41

Table 3
(Continued)

Fea. No.	x -offset ^a (mas)	δx^b (mas)	y -offset ^c (mas)	δy (mas)	μ_x^d (mas yr ⁻¹)	$\delta\mu_x^{+e}$ (mas yr ⁻¹)	$\delta\mu_x^{-f}$ (mas yr ⁻¹)	μ_y^g (mas yr ⁻¹)	$\delta\mu_y^{+}$ (mas yr ⁻¹)	$\delta\mu_y^{-}$ (mas yr ⁻¹)	V_{LSR}^h (km s ⁻¹)	δV_{LSR}^i (km s ⁻¹)
26	498.683	0.037	-246.268	0.012	-1.733	0.000	-1.091	-1.264	1.628	0.000	7.75	0.05
27	507.479	0.044	-248.436	0.024	-2.687	0.170	-1.388	-2.305	2.080	0.000	6.33	0.09
28	511.586	0.073	-241.419	0.045	-3.984	1.015	-2.233	0.888	2.471	0.000	10.20	0.17
29	540.823	0.002	-221.204	0.008	2.988	1.079	-2.297	7.855	5.782	-3.07	-216.55	0.22
30	539.921	0.102	-220.185	0.823	0.272	3.239	-4.456	-0.719	23.403	-20.69	-224.27	0.49
31	485.458	0.047	-121.971	0.015	0.074	0.920	-2.137	-0.366	1.832	0.000	9.32	0.11
32	502.853	0.016	-114.478	0.018	3.211	0.046	-1.263	0.664	1.861	0.000	-7.26	0.28
33	498.500	0.140	-115.006	0.142	-2.132	3.324	-4.541	1.610	4.665	-1.953	-10.82	0.06
34	489.305	0.103	-41.987	0.123	-0.489	2.182	-3.4	0.115	4.467	-1.754	-55.14	0.23
35	501.720	0.053	15.949	0.018	-1.504	1.252	-2.469	1.084	2.397	0.000	-115.06	0.62
36	502.056	0.010	16.331	0.008	2.277	0.000	-0.995	4.287	1.659	0.000	-125.19	0.28
37	552.683	0.001	-192.032	0.004	-5.354	0.299	-1.517	-5.973	2.509	0.000	-34.54	0.08
38	552.561	0.244	-200.415	0.177	-2.43	0.773	-1.99	-1.459	2.388	0.000	-102.31	0.13
39	664.675	0.002	235.167	0.001	0.286	0.000	-0.817	-1.549	1.463	0.000	9.81	0.12
40	657.313	0.006	225.868	0.015	-0.266	0.000	-0.646	-0.342	1.400	0.000	-19.52	0.27
41	658.998	0.003	226.167	0.012	-0.515	0.000	-0.75	-1.651	1.767	0.000	-30.98	0.30
42	659.203	0.004	226.300	0.011	-1.271	0.000	-0.766	-1.291	1.804	0.000	-38.77	0.60
43	662.334	0.025	228.068	0.011	-0.959	0.000	-1.078	-1.162	1.620	0.000	-49.83	0.24
44	706.619	0.104	170.984	0.054	1.205	2.693	-3.91	5.970	3.116	-0.403	-171.32	0.07
45	950.102	0.083	-171.755	0.259	-1.013	1.829	-3.047	2.011	8.341	-5.629	-70.92	0.80
46	942.333	0.443	-165.153	0.179	8.162	11.212	-12.429	0.856	6.316	-3.604	-78.98	0.09
47	950.079	0.062	-169.172	0.085	2.648	1.064	-2.282	2.391	3.535	-0.822	-88.35	0.58
48	1076.052	0.018	-246.588	0.016	-1.558	0.303	-1.52	-0.995	2.152	0.000	-32.06	0.28
49	1076.544	0.012	-247.042	0.010	-0.587	0.000	-1.132	0.549	1.781	0.000	-46.82	0.49
50	1239.304	0.018	324.982	0.015	4.105	0.452	-1.67	0.719	2.129	0.000	6.42	0.53
51	1332.819	0.006	378.440	0.014	0.752	0.000	-0.731	0.287	1.453	0.000	12.45	0.06
52	1322.296	0.060	370.273	0.020	0.592	0.750	-1.968	1.190	1.890	0.000	10.88	0.34
53	1325.849	0.023	370.213	0.023	-1.441	0.000	-1.194	3.667	2.036	0.000	8.29	0.33
54	1718.307	0.040	145.881	0.051	-1.705	0.429	-1.646	2.880	2.634	0.000	13.43	0.49
55	1722.547	0.006	144.712	0.001	0.826	0.000	-0.868	0.574	1.433	0.000	10.18	0.08
56	1723.885	0.068	154.021	0.092	11.403	1.141	-2.358	-1.621	3.527	-0.815	10.14	0.24
57	1697.819	0.007	191.944	0.020	2.683	0.000	-0.897	1.229	1.914	0.000	8.08	0.25
58	1757.559	0.006	82.555	0.006	1.14	0.000	-0.795	-0.264	1.535	0.000	8.49	0.15
59	532.533	0.019	-176.036	0.025	-0.336	0.232	-1.45	-0.724	2.228	0.000	49.91	0.06
60	527.544	0.097	-171.246	0.045	-0.263	0.000	-0.977	-0.398	1.859	0.000	26.37	0.19
61	724.355	0.561	785.210	0.477	0.654	13.319	-14.537	0.911	12.707	-9.994	63.49	0.21
62	825.800	0.046	-51.447	0.023	-0.144	0.548	-1.765	-0.555	2.082	0.000	43.23	0.18
63	1064.559	0.283	-1736.21	9.000	-2.402	7.266	-8.483	-8.98	12.579	-9.866	50.80	0.60
64	1140.167	0.034	-1658.17	6.000	0.221	0.420	-1.637	-2.058	1.876	0.000	46.63	0.13
65	1111.737	0.020	-1538.62	7.000	-1.129	0.371	-1.589	-5.251	3.099	-0.387	123.10	0.79
66	1133.475	0.003	81.429	0.002	0.964	0.000	-0.723	-0.562	1.432	0.000	122.70	0.16
67	1135.391	0.110	103.145	0.043	0.639	2.734	-3.951	-0.729	2.684	0.000	92.25	0.04
68	1087.985	0.114	305.873	0.114	1.304	2.590	-3.808	-0.45	4.591	-1.878	159.65	0.82
69	1086.930	0.166	307.737	0.230	-0.44	6.107	-7.324	0.047	9.482	-6.77	137.30	0.60
70	1138.052	0.028	1245.849	0.034	1.447	0.000	-1.137	3.153	2.228	0.000	62.77	0.05
71	1219.663	0.111	244.764	0.116	1.158	1.790	-3.007	-0.393	4.553	-1.84	68.18	0.15
72	1231.024	0.369	238.017	0.463	-0.004	0.132	-1.35	3.119	10.531	-7.819	56.24	0.24
73	1222.031	0.355	227.865	0.512	-1.43	10.974	-12.192	-3.093	16.797	-14.085	54.17	0.09
74	1221.690	0.447	252.210	0.248	3.402	10.933	-12.15	12.368	9.047	-6.334	68.06	0.12
75	1231.335	0.004	436.655	0.030	1.269	0.000	-0.816	0.534	2.246	0.000	184.51	0.13
76	1220.414	0.003	436.395	0.003	0.536	0.000	-0.776	0.582	1.529	0.000	130.76	0.19
77	1203.220	0.094	961.278	0.104	7.556	2.878	-4.096	11.413	6.044	-3.331	81.11	0.17
78	1196.457	0.223	952.303	0.104	-2.121	6.072	-7.289	-1.246	4.165	-1.452	80.75	0.25
79	1270.133	0.058	153.541	0.145	1.491	0.938	-2.155	-5.085	3.899	-1.186	34.98	0.94
80	1284.911	0.045	882.977	0.007	1.282	0.641	-1.858	1.107	1.588	0.000	38.24	0.81
81	1276.669	0.021	890.469	0.024	0.798	0.037	-1.254	2.016	2.113	0.000	31.81	0.26
82	1279.855	0.006	888.173	0.009	0.489	0.000	-0.763	0.749	1.595	0.000	28.83	0.50
83	1307.764	0.027	936.188	0.016	1.674	0.170	-1.388	1.312	1.782	0.000	27.24	0.15
84	1291.400	0.011	1122.479	0.033	0.772	0.000	-1.049	2.147	2.656	0.000	84.93	0.38
85	1447.428	0.051	-52.262	0.048	2.935	0.388	-1.606	1.111	2.613	0.000	26.68	0.44
86	1494.268	0.017	169.891	0.016	1.037	0.000	-0.757	0.776	2.020	0.000	54.37	0.12
87	1634.888	0.114	26.580	0.027	1.737	2.476	-3.694	-0.077	2.173	0.000	76.38	0.78
88	1655.746	0.300	24.558	0.147	-3.707	4.391	-5.608	-0.845	5.170	-2.458	64.32	0.31

Table 3
(Continued)

Fea. No.	x -offset ^a (mas)	δx ^b (mas)	y -offset ^c (mas)	δy (mas)	μ_x ^d (mas yr ⁻¹)	$\delta\mu_x^+$ ^e (mas yr ⁻¹)	$\delta\mu_x^-$ ^f (mas yr ⁻¹)	μ_y ^g (mas yr ⁻¹)	$\delta\mu_y^+$ (mas yr ⁻¹)	$\delta\mu_y^-$ (mas yr ⁻¹)	V_{LSR}^h (km s ⁻¹)	δV_{LSR}^i (km s ⁻¹)
89	1718.684	0.038	114.092	0.036	0.582	1.122	-2.34	0.165	3.011	-0.299	121.03	0.21
90	1715.487	0.007	106.876	0.011	1.718	0.697	-1.914	-0.028	1.952	0.000	119.07	0.35
91	1723.246	0.134	111.461	0.058	0.983	3.502	-4.719	0.132	2.971	-0.259	106.89	0.38
92	1723.252	0.238	104.675	0.109	3.284	5.850	-7.067	0.395	3.487	-0.774	81.92	0.52
93	1704.735	0.179	79.880	0.080	1.305	3.251	-4.469	0.805	3.243	-0.531	46.80	0.09
94	1719.319	0.013	78.849	0.042	1.236	0.000	-0.973	-0.557	2.063	0.000	39.54	0.00
95	1731.049	0.013	100.917	0.034	1.484	0.000	-0.946	-0.249	2.089	0.000	16.33	0.18
96	1726.926	0.035	189.765	0.030	2.101	0.387	-1.604	0.250	2.235	0.000	199.92	0.10
97	1666.534	0.082	281.312	0.089	2.009	1.151	-2.368	-1.349	4.307	-1.595	145.44	0.08
98	1796.173	0.016	17.537	0.013	1.041	0.000	-0.695	-0.595	1.399	0.000	18.26	0.30
99	1794.870	0.043	143.660	0.061	2.331	0.733	-1.95	0.468	3.155	-0.442	208.47	0.80
100	1811.797	0.013	136.459	0.008	5.727	0.035	-1.253	1.886	1.720	0.000	184.22	1.04
101	1835.315	0.539	141.304	0.152	1.208	9.863	-11.081	0.468	4.922	-2.209	168.55	0.34
102	2005.809	0.015	503.030	0.017	2.518	0.000	-1.207	0.655	1.756	0.000	140.24	0.10

Notes. The offset position in each maser feature corresponds with the reference position at R.A. (J2000) $19^{\text{h}}10^{\text{m}}13^{\text{s}}.41$, decl. (J2000) $+09^{\circ}06'14''.3$.

^a R.A. offset from the reference position.

^b The positional uncertainties in each feature are calculated from the standard deviation of the position of the components in each feature.

^c Decl. offset from the reference position.

^d Proper motion in the east–west direction.

^e Maximum uncertainty of proper motion in each direction.

^f Minimum uncertainty of proper motion in each direction.

^g Proper motion in the north–south direction.

^h Velocity with respect to the LSR, assuming a rest frequency of 22.235080 GHz.

ⁱ The uncertainties of the LSR velocities are calculated from the standard deviation of their LSR velocities.

To compare the maser position offsets of KaVA with the high-accuracy VLBA data obtained from Zhang et al. (2013), however, each offset will be shifted with the value of $(-516.464, +111.798)$ mas, i.e., R.A. and decl. offset, respectively.

Table 4
Proper Motion of H₂O Maser Features Calculated from Linear Fitting

Fea. No.	x -offset ^a (mas)	δx ^b (mas)	y -offset ^c (mas)	δy (mas)	μ_x ^d (mas yr ⁻¹)	$\delta\mu_x^e$ (mas yr ⁻¹)	μ_y^f (mas yr ⁻¹)	$\delta\mu_y^g$ (mas yr ⁻¹)	V_{LSR}^h (km s ⁻¹)	δV_{LSR}^i (km s ⁻¹)
1	-1638.531	0.089	-83.855	0.032	0.735	0.533	-0.204	0.170	5.06	0.31
2	19.138	0.003	-213.446	0.005	-1.073	0.088	-0.307	0.085	-74.00	0.23
3	0.690	0.050	-0.156	0.018	-1.073	0.088	-0.898	0.140	0.38	0.21
4	9.409	0.023	-6.941	0.025	1.995	0.240	-3.367	0.296	-4.78	0.05
5	12.045	0.010	-7.016	0.093	-0.664	0.300	0.716	0.818	-13.68	0.13
6	5.576	0.009	-13.332	0.002	-2.377	0.151	-0.723	0.183	-21.94	0.21
7	-10.302	0.011	-9.319	0.007	1.984	0.327	-0.723	0.398	-32.55	0.26
8	-14.523	0.043	-25.361	0.022	-0.726	0.229	-0.609	0.119	-63.56	1.32
9	-22.183	0.066	-23.541	0.010	-2.665	0.519	-1.237	0.124	-69.05	1.07
10	6.952	0.022	-23.630	0.014	-1.643	0.121	-0.186	0.083	-86.27	0.12
11	20.247	0.011	-11.813	0.009	-1.047	0.061	-0.577	0.063	-91.72	0.24
12	-5.678	0.026	-27.289	0.015	-5.357	0.796	0.924	0.621	-104.93	0.92
13	-8.905	0.039	-24.940	0.055	-1.902	0.287	0.723	0.486	-106.83	0.20
14	7.147	0.020	-27.615	0.024	-2.154	0.117	-0.911	0.124	-123.66	0.48
15	50.641	0.349	-5.896	0.757	-0.463	2.988	3.174	6.874	-134.28	0.99
16	24.975	0.297	-44.737	0.301	-3.531	2.005	-0.549	1.556	-153.24	0.55
17	38.237	0.013	-18.700	0.016	-1.745	0.218	-0.521	0.155	-159.15	0.17
18	104.643	0.062	24.230	0.162	-1.314	0.712	-0.117	1.074	-100.96	0.59
19	55.385	0.243	-3.712	0.180	0.444	1.227	-1.402	0.913	-145.42	0.23
20	88.388	0.188	80.431	0.031	-2.537	1.326	-0.201	0.244	-118.02	0.56
21	224.568	0.080	-66.880	0.025	1.871	0.562	0.417	0.181	-19.55	0.50
22	486.535	0.003	-454.412	0.005	-0.616	0.036	-0.921	0.062	-13.63	0.38
23	498.497	0.015	-415.696	0.022	-0.079	0.210	-1.804	0.240	-43.19	0.19
24	538.492	0.263	-250.292	0.321	-8.279	1.848	-0.680	1.644	-47.33	0.52
25	514.292	0.136	-274.890	0.032	-0.594	0.745	-1.086	0.238	-201.07	0.41
26	498.683	0.037	-246.268	0.012	-1.628	0.135	-1.267	0.062	7.75	0.05

Table 4
(Continued)

Fea. No.	x -offset ^a (mas)	δx^b (mas)	y -offset ^c (mas)	δy (mas)	μ_x^d (mas yr ⁻¹)	$\delta\mu_x^e$ (mas yr ⁻¹)	μ_y^f (mas yr ⁻¹)	$\delta\mu_y^g$ (mas yr ⁻¹)	V_{LSR}^h (km s ⁻¹)	δV_{LSR}^i (km s ⁻¹)
27	507.479	0.044	-248.436	0.024	-2.048	0.257	-2.520	0.179	6.33	0.09
28	511.586	0.073	-241.419	0.045	-5.843	0.420	2.046	0.260	10.20	0.17
29	540.823	0.002	-221.204	0.008	-0.927	0.811	-2.023	2.115	-216.55	0.22
30	539.921	0.102	-220.185	0.823	-1.299	1.187	0.194	5.278	-224.27	0.49
31	485.458	0.047	-121.971	0.015	0.954	0.402	-0.556	0.118	9.32	0.11
32	502.853	0.016	-114.478	0.018	1.360	0.219	0.661	0.105	-7.26	0.28
33	498.500	0.140	-115.006	0.142	-3.067	0.997	3.813	0.877	-10.82	0.06
34	489.305	0.103	-41.987	0.123	-0.594	0.610	0.534	0.617	-55.14	0.23
35	501.720	0.053	15.949	0.018	-1.062	0.559	0.234	0.446	-115.06	0.62
36	502.056	0.010	16.331	0.008	-0.434	0.136	-0.193	0.093	-125.19	0.28
37	552.683	0.001	-192.032	0.004	-0.865	0.394	0.143	0.511	-34.54	0.08
38	552.561	0.244	-200.415	0.177	-6.409	0.519	-2.812	0.354	-102.31	0.13
39	664.675	0.002	235.167	0.001	0.331	0.085	-0.756	0.050	9.81	0.12
40	657.313	0.006	225.868	0.015	-1.252	0.014	-0.157	0.014	-19.52	0.27
41	658.998	0.003	226.167	0.012	0.418	0.047	0.303	0.108	-30.98	0.30
42	659.203	0.004	226.300	0.011	0.312	0.050	-0.080	0.126	-38.77	0.60
43	662.334	0.025	228.068	0.011	-0.857	0.125	-0.142	0.057	-49.83	0.24
44	706.619	0.104	170.984	0.054	-0.236	0.804	0.544	0.460	-171.32	0.07
45	950.102	0.083	-171.755	0.259	-1.036	0.511	1.721	1.399	-70.92	0.80
46	942.333	0.443	-165.153	0.179	3.873	2.911	-1.709	0.972	-78.98	0.09
47	950.079	0.062	-169.172	0.085	0.775	0.359	-0.182	0.449	-88.35	0.58
48	1076.052	0.018	-246.588	0.016	-0.583	0.353	-0.255	0.303	-32.06	0.28
49	1076.544	0.012	-247.042	0.010	-0.284	0.190	0.029	0.155	-46.82	0.49
50	1239.304	0.018	324.982	0.015	4.610	0.384	-0.394	0.282	6.42	0.53
51	1332.819	0.006	378.440	0.014	0.415	0.028	0.928	0.028	12.45	0.06
52	1322.296	0.060	370.273	0.020	-0.521	0.277	1.366	0.099	10.88	0.34
53	1325.849	0.023	370.213	0.023	-2.026	0.126	4.391	0.158	8.29	0.33
54	1718.307	0.040	145.881	0.051	0.070	0.196	1.169	0.245	13.43	0.49
55	1722.547	0.006	144.712	0.001	0.578	0.087	0.238	0.029	10.18	0.08
56	1723.885	0.068	154.021	0.092	9.015	0.376	-4.752	0.468	10.14	0.24
57	1697.819	0.007	191.944	0.020	2.437	0.096	-0.881	0.001	8.08	0.25
58	1757.559	0.006	82.555	0.006	0.834	0.047	0.011	0.044	8.49	0.15
59	532.533	0.019	-176.036	0.025	0.102	0.211	0.234	0.230	49.91	0.06
60	527.544	0.097	-171.246	0.045	-0.868	0.130	0.099	0.165	26.37	0.19
61	724.355	0.561	785.210	0.477	0.761	3.594	1.118	2.937	63.49	0.21
62	825.800	0.046	-51.447	0.023	-0.467	0.272	0.022	0.183	43.23	0.18
63	1064.559	0.283	-1736.219	0.471	-1.427	2.045	-7.195	2.546	50.80	0.60
64	1140.167	0.034	-1658.176	0.017	0.258	0.242	-1.369	0.126	46.63	0.13
65	1111.737	0.020	-1538.627	0.073	-1.109	0.309	-4.956	0.398	123.10	0.79
66	1133.475	0.003	81.429	0.002	0.936	0.035	-0.175	0.020	122.70	0.16
67	1135.391	0.110	103.145	0.043	0.642	0.844	-0.467	0.337	92.25	0.04
68	1087.985	0.114	305.873	0.114	1.181	0.778	-0.292	0.763	159.65	0.82
69	1086.930	0.166	307.737	0.230	1.009	1.720	-0.500	2.148	137.30	0.60
70	1138.052	0.028	1245.849	0.034	1.254	0.125	3.426	0.215	62.77	0.05
71	1219.663	0.111	244.764	0.116	0.907	0.519	0.059	0.577	68.18	0.15
72	1231.024	0.369	238.017	0.463	0.244	0.288	2.557	2.509	56.24	0.24
73	1222.031	0.355	227.865	0.512	-0.441	3.043	3.905	3.875	54.17	0.09
74	1221.690	0.447	252.210	0.248	1.469	2.707	6.235	1.939	68.06	0.12
75	1231.335	0.004	436.655	0.030	1.626	0.057	0.928	0.220	184.51	0.13
76	1220.414	0.003	436.395	0.003	0.574	0.048	0.873	0.052	130.76	0.19
77	1203.220	0.094	961.278	0.104	0.021	1.096	-0.179	1.709	81.11	0.17
78	1196.457	0.223	952.303	0.104	1.334	1.695	1.111	0.544	80.75	0.25
79	1270.133	0.058	153.541	0.145	1.546	0.373	-4.912	0.599	34.98	0.94
80	1284.911	0.045	882.977	0.007	1.301	0.228	1.469	0.057	38.24	0.81
81	1276.669	0.021	890.469	0.024	-0.061	0.156	1.381	0.192	31.81	0.26
82	1279.855	0.006	888.173	0.009	0.483	0.039	1.063	0.050	28.83	0.50
83	1307.764	0.027	936.188	0.016	1.436	0.198	0.968	0.109	27.24	0.15
84	1291.400	0.011	1122.479	0.033	1.152	0.129	2.148	0.345	84.93	0.38
85	1447.428	0.051	-52.262	0.048	2.350	0.291	0.062	0.339	26.68	0.44
86	1494.268	0.017	169.891	0.016	0.561	0.056	0.618	0.155	54.37	0.12
87	1634.888	0.114	26.580	0.027	2.649	0.705	0.460	0.161	76.38	0.78
88	1655.746	0.300	24.558	0.147	-3.816	1.340	-0.900	0.789	64.32	0.31
89	1718.684	0.038	114.092	0.036	1.729	0.409	0.022	0.380	121.03	0.21

Table 4
(Continued)

Fea. No.	x -offset ^a (mas)	δx^b (mas)	y -offset ^c (mas)	δy (mas)	μ_x^d (mas yr ⁻¹)	$\delta\mu_x^e$ (mas yr ⁻¹)	μ_y^f (mas yr ⁻¹)	$\delta\mu_y^e$ (mas yr ⁻¹)	V_{LSR}^g (km s ⁻¹)	δV_{LSR}^h (km s ⁻¹)
90	1715.487	0.007	106.876	0.011	1.199	0.603	0.190	0.233	119.07	0.35
91	1723.246	0.134	111.461	0.058	1.192	1.041	0.398	0.384	106.89	0.38
92	1723.252	0.238	104.675	0.109	3.555	1.523	0.910	0.588	81.92	0.52
93	1704.735	0.179	79.880	0.080	1.020	1.019	1.626	0.471	46.80	0.09
94	1719.319	0.013	78.849	0.042	1.100	0.094	-0.095	0.209	39.54	0.00
95	1731.049	0.013	100.917	0.034	1.323	0.080	0.344	0.184	16.33	0.18
96	1726.926	0.035	189.765	0.030	2.134	0.225	0.435	0.202	199.92	0.10
97	1666.534	0.082	281.312	0.089	1.959	0.504	-2.242	0.756	145.44	0.08
98	1796.173	0.016	17.537	0.013	0.540	0.030	0.088	0.017	18.26	0.30
99	1794.870	0.043	143.660	0.061	1.856	0.339	0.460	0.446	208.47	0.80
100	1811.797	0.013	136.459	0.008	2.361	0.162	0.146	0.083	184.22	1.04
101	1835.315	0.539	141.304	0.152	-0.609	3.291	1.238	0.997	168.55	0.34
102	2005.809	0.015	503.030	0.017	2.466	0.158	1.019	0.115	140.24	0.10

Note. The offset position in each maser feature corresponds with the reference position at R.A. (J2000) 19^h10^m13^s.41, decl. (J2000) +09°06′14″.3.

^a R.A. offset from the reference position.

^b The positional uncertainties in each feature are calculated from the standard deviation of the position of the components in each feature.

^c Decl. offset from the reference position.

^d Proper motion in the east–west direction.








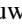
^e Uncertainty of proper motion in each direction, i.e., east–west and north–south.

^f Proper motion in the north–south direction.

^g Velocity with respect to the LSR, assuming a rest frequency of 22.235080 GHz.

^h The uncertainties of the LSR velocities are calculated from the standard deviation of their LSR velocities.

ORCID iDs

Kitiyanee Asanok  <https://orcid.org/0000-0002-4125-0941>
 Malcolm D. Gray  <https://orcid.org/0000-0002-2094-846X>
 Tomoya Hirota  <https://orcid.org/0000-0003-1659-095X>
 Koichiro Sugiyama  <https://orcid.org/0000-0002-6033-5000>
 Busaba H. Kramer  <https://orcid.org/0000-0001-8168-5141>
 Tie Liu  <https://orcid.org/0000-0002-5286-2564>
 Kee-Tae Kim  <https://orcid.org/0000-0003-2412-7092>
 Bannawit Pimpanuwat  <https://orcid.org/0000-0001-8782-0754>

References

- Boboltz, D. A., Simonetti, J. H., Dennison, B., Diamond, P. J., & Uphoff, J. A. 1998, *ApJ*, **509**, 256
- Burke, B. F., Papa, D. C., Papadopoulos, G. D., et al. 1970, *ApJL*, **160**, L63
- Cesaroni, R., Palagi, F., Felli, M., et al. 1988, *A&AS*, **76**, 445
- Cheung, A. C., Rank, D. M., Townes, C. H., Thornton, D. D., & Welch, W. J. 1969, *Natur*, **221**, 626
- Crowther, P. A., Schnurr, O., Hirschi, R., et al. 2010, *MNRAS*, **408**, 731
- De Pree, C. G., Wilner, D. J., Goss, W. M., Welch, W. J., & McGrath, E. 2000, *ApJ*, **540**, 308
- De Pree, C. G., Wilner, D. J., Mercer, A. J., et al. 2004, *ApJ*, **600**, 286
- Dreher, J. W., Johnston, K. J., Welch, W. J., & Walker, R. C. 1984, *ApJ*, **283**, 632
- Gray, M. 2012, *Maser Sources in Astrophysics*, Cambridge Astrophysics (Cambridge: Cambridge Univ. Press)
- Greisen, E. W. 2003, *Information Handling in Astronomy - Historical Vistas*, Vol. 285 (1st edn.; Dordrecht: Kluwer Academic), 109
- Gwinn, C. R., Moran, J. M., & Reid, M. J. 1992, *ApJ*, **393**, 149
- Honma, M., Yoon, K. C., Bushimata, T., et al. 2004, *PASJ*, **56**, L15
- Liljeström, T., & Gwinn, C. R. 2000, *ApJ*, **534**, 781
- Mac Low, M.-M., & Elitzur, M. 1992, *ApJL*, **393**, L33
- Mezger, P. G., Schraml, J., & Terzian, Y. 1967, *ApJ*, **150**, 807
- Phetra, M., Asanok, K., Hirota, T., et al. 2019, *JPhCS*, **1380**, 012055
- Press, W. H., Teukolsky, S. A., & Vetterling, W. T. 1997, *Fortran Numerical Recipes*, Vol. 2, *Numerical Recipes in FORTRAN90: The Art of Parallel Scientific Computing* (2nd edn.; Cambridge: Cambridge Univ. Press)
- Rogers, A. E. E. 1976, *MExP*, **12**, 139
- Thompson, A. R., Moran, J. M., & Swenson, G. W. 2017, *Interferometry and Synthesis in Radio Astronomy* (Cham: Springer)
- Volvach, A. E., Volvach, L. N., & Larionov, M. G. 2020, *MNRAS Lett.*, **496**, L147
- Volvach, L. N., Volvach, A. E., Larionov, M. G., MacLeod, G. C., & Wolak, P. 2019a, *MNRAS Lett.*, **487**, L77
- Volvach, L. N., Volvach, A. E., Larionov, M. G., et al. 2019b, *A&A*, **628**, A89
- Zhang, B., Reid, M. J., Menten, K. M., et al. 2013, *ApJ*, **775**, 79
- Zhou, J. J., Zheng, X. W., & Chen, Y. X. 2002, *A&A*, **390**, 281